



Synergistic Structure and Iron-Vacancy Engineering Realizing High Initial Coulombic Efficiency and Kinetically Accelerated Lithium Storage in Lithium Iron Oxide

Wu, Naiteng; Shen, Jinke; Yong, Kai; Chen, Chengqian; Li, Jian; Xie, Yi; Guo, Donglei; Liu, Guilong; Li, Jin; Cao, Ang

Total number of authors:
13

Published in:
Advanced Science

Link to article, DOI:
[10.1002/adv.202206574](https://doi.org/10.1002/adv.202206574)

Publication date:
2023

Document Version
Publisher's PDF, also known as Version of record

[Link back to DTU Orbit](#)

Citation (APA):

Wu, N., Shen, J., Yong, K., Chen, C., Li, J., Xie, Y., Guo, D., Liu, G., Li, J., Cao, A., Liu, X., Mi, H., & Wu, H. (2023). Synergistic Structure and Iron-Vacancy Engineering Realizing High Initial Coulombic Efficiency and Kinetically Accelerated Lithium Storage in Lithium Iron Oxide. *Advanced Science*, 10(9), Article 2206574. <https://doi.org/10.1002/adv.202206574>

General rights

Copyright and moral rights for the publications made accessible in the public portal are retained by the authors and/or other copyright owners and it is a condition of accessing publications that users recognise and abide by the legal requirements associated with these rights.

- Users may download and print one copy of any publication from the public portal for the purpose of private study or research.
- You may not further distribute the material or use it for any profit-making activity or commercial gain
- You may freely distribute the URL identifying the publication in the public portal

If you believe that this document breaches copyright please contact us providing details, and we will remove access to the work immediately and investigate your claim.

Synergistic Structure and Iron-Vacancy Engineering Realizing High Initial Coulombic Efficiency and Kinetically Accelerated Lithium Storage in Lithium Iron Oxide

Naiteng Wu, Jinke Shen, Kai Yong, Chengqian Chen, Jian Li, Yi Xie, Donglei Guo, Guilong Liu, Jin Li, Ang Cao, Xianming Liu,* Hongyu Mi,* and Hao Wu*

Transition metal oxides with high capacity still confront the challenges of low initial coulombic efficiency (ICE, generally <70%) and inferior cyclic stability for practical lithium-storage. Herein, a hollow slender carambola-like $\text{Li}_{0.43}\text{FeO}_{1.51}$ with Fe vacancies is proposed by a facile reaction of Fe^{3+} -containing metal-organic frameworks with Li_2CO_3 . Synthesis experiments combined with synchrotron-radiation X-ray measurements identify that the hollow structure is caused by Li_2CO_3 erosion, while the formation of Fe vacancies is resulted from insufficient lithiation process with reduced Li_2CO_3 dosage. The optimized lithium iron oxides exhibit remarkably improved ICE (from 68.24% to 86.78%), high-rate performance (357 mAh g^{-1} at 5 A g^{-1}), and superior cycling stability (884 mAh g^{-1} after 500 cycles at 0.5 A g^{-1}). Paring with LiFePO_4 cathodes, the full-cells achieve extraordinary cyclic stability with 99.3% retention after 100 cycles. The improved electrochemical performances can be attributed to the synergy of structural characteristics and Fe vacancy engineering. The unique hollow structure alleviates the volume expansion of $\text{Li}_{0.43}\text{FeO}_{1.51}$, while the in situ generated Fe vacancies are powerful for modulating electronic structure with boosted Li^+ transport rate and catalyze more Li_2O decomposition to react with Fe in the first charge process, hence enhancing the ICE of lithium iron oxide anode materials.

1. Introduction

Lithium-ion batteries (LIBs) have been widely used in energy storage fields because of their high energy density and long cycle life.^[1,2] With the increasing requirements in electric vehicles, hybrid electric vehicles, and intelligent housing systems, next-generation LIBs with higher energy density and longer cycle life are required. In the field of anode materials, transition metal oxides with typical conversion reactions enable a high theoretical capacity, which is 2–3 times higher than that of commercial graphite. Among many transition metal oxides, iron-based oxides have attracted extensive research owing to their high theoretical capacity (1007 mAh g^{-1}), high volumetric capacity, low price, and nontoxicity.^[3,4] It's worth noting that the lithiation process of iron oxide leads to low initial coulombic efficiency (ICE), poor reversibility, and cyclic stability, which would be ascribed to the extra lithium consumption during the

N. Wu, J. Shen, C. Chen, J. Li, Y. Xie, D. Guo, G. Liu, J. Li, X. Liu
Key Laboratory of Function-oriented Porous Materials of Henan Province
College of Chemistry and Chemical Engineering
Luoyang Normal University
Luoyang, Henan 471934, P. R. China
E-mail: lxm-nanoenergy@lynu.edu.cn

J. Shen, H. Mi
State Key Laboratory of Chemistry and Utilization of Carbon Based
Energy Resources
School of Chemical Engineering and Technology
Xinjiang University
Urumqi, Xinjiang 830046, P. R. China
E-mail: mmihongyu@xju.edu.cn

K. Yong, H. Wu
Engineering Research Center of Alternative Energy Materials & Devices
Ministry of Education
College of Materials Science and Engineering
Sichuan University
Chengdu, Sichuan 610065, P. R. China
E-mail: hao.wu@scu.edu.cn

A. Cao
Department of Physics
Technical University of Denmark
Lyngby 2800, Denmark



The ORCID identification number(s) for the author(s) of this article can be found under <https://doi.org/10.1002/advs.202206574>

© 2023 The Authors. Advanced Science published by Wiley-VCH GmbH. This is an open access article under the terms of the Creative Commons Attribution License, which permits use, distribution and reproduction in any medium, provided the original work is properly cited.

DOI: 10.1002/advs.202206574

formation of solid electrolyte interface (SEI) film and partially irreversible Li_2O , inferior ion/electron transportation, and unavoidable volumetric expansion, respectively.^[5,6]

Rational design of nanostructures^[7–9] and carbon modification/construction of composite materials^[10–12] are the common strategies to improve the lithium storage performance of iron-based anodes. Liu et al. designed a carbon-coated $\alpha\text{-Fe}_2\text{O}_3@\text{Fe}_3\text{O}_4$ heterostructure, which endowed a reversible capacity of 711 mAh g^{-1} after 200 cycles.^[13] Heterogeneous mesoporous $\text{Mn}_2\text{O}_3/\text{Fe}_2\text{O}_3$ showed a high reversible capacity (750 mAh g^{-1} at 1 A g^{-1}) and long-term cyclic life (85.2% after 500 cycles).^[14] Core-shell structure improved the conductivity and cyclic stability of $\text{Fe}_2\text{O}_3/\text{C}$, which delivered a reversible capacity of 681 mAh g^{-1} after 300 cycles at 1 A g^{-1} .^[15] Besides, the introduction of lattice defects (mostly oxygen vacancy for metal oxides) by alien or different valence ion doping,^[16–18] purposeful etching,^[19,20] and designing nonstoichiometric compound,^[21,22] is another effective route to increase the electronic and ionic conductivity of electrode materials.^[23] Our previous works had also been encouraged by this strategy to improve the electrochemical performances of TiO_2 ,^[24–26] CoO ,^[27] SnO_2 ,^[28] MoO_2 ,^[29] and V_2O_5 .^[30] Creation of cationic vacancies is more difficult than that of anionic defects, because of the higher formation energy and complex formation process.^[31–33] However, the above-mentioned works don't alleviate the additional consumption of lithium during the solid electrode interface (SEI) film formation, resulting in a low ICE (usually lower than 70%). Nowadays, prelithiation is considered as an effective route to increase the ICE of alloying/de-alloying anode materials. Zhao et al. reported that the ICE of nano-Si increased from 76% to 94% after partial prelithiation process.^[34] Such prelithiated route also inspired the research of iron oxide materials. Unfortunately, there are no obvious improvements in ICE, and the ICE of the optimal sample is generally lower than 70%.^[35,36] LiH has been carried out as a powerful chemical prelithiated reagent to increase the ICE of Si/SiO_x -based materials through the high-temperature solid-state reaction with their precursors.^[37,38] Due to its strong reducibility, high price (almost five times than the common lithium salt), and flammability, LiH would be unsuitable for large-scale applications. Besides, other chemical prelithiation reagents, such as low-potential Li-containing chemicals (*n*-butyl lithium, lithium naphthalene, biphenyl lithium, and lithium-9,9-dimethylfluorene)^[39,40] and Li-rich additives ($\text{Li}_x\text{Si}^{[41]}$ and $\text{Li}_x\text{Sn}^{[42]}$ alloys), also face the problems of oxygen and moisture sensitivity and high cost. Another way to improve the ICE is to decrease the irreversibility of Li_2O during the first charge process. According to the literatures on electrocatalysis, the cationic vacancies in the electrode materials promoted the decomposition of lithium oxides,^[43–45] which would be carried out to stimulate the reactivity of irreversible Li_2O . Unfortunately, there are very few reports on the enhancement of ICE from this perspective. Therefore, it remains a significant challenge to seek a green and scalable route to improve the ICE and electrochemical performances of iron oxides.

In this work, a type of hollow slender carambola-like lithium iron oxide ($\text{Li}_{0.43}\text{FeO}_{1.51}$, denoted as LFO-0.01) with Fe vacancies has been synthesized by a facile chemical reaction of MIL-88A(Fe) with Li_2CO_3 at 600°C under Ar atmosphere (Figure 1a). Metal-organic framework (MOF) precursor not only provides a

slender carambola-like template and porous structure, but also ensures the carbon layer derived from organic groups to increase the conductivity. Interestingly, when a small amount of Li_2CO_3 is adopted during the heat-treatment process, it can simultaneously result in the formation of hollow (caused by lithium erosion) and Fe vacancies (induced by insufficient lithiation process) in the lithium iron oxide. As unveiled by X-ray absorption fine structure and density functional theory (DFT) calculations, the presence of Fe vacancies is capable of accelerating the transport rate of lithium ions and catalyzing more decomposition of Li_2O to react with Fe in the first charge process, consequently delivering the improved ICE. When used as anode material for LIBs, the resultant LFO-0.01 exhibits higher reversible capacity (979 mAh g^{-1} at 0.05 A g^{-1}), highest ICE (86.78%), best cycling stability (884 mAh g^{-1} after 500 cycles at 0.5 A g^{-1}), and high-rate performance than that of the counterparts. Moreover, the $\text{LiFePO}_4||\text{LFO-0.01}$ coin full-cells deliver a high capacity (131 mAh g^{-1} , calculated based on the weight of the cathode material) and remarkable cyclic stability of the 99.3% retention after 100 cycles.

2. Results and Discussions

The phase compositions of as-prepared samples were detected through X-ray diffraction (XRD). As shown in Figure S1a (Supporting Information), after direct pyrolysis of MIL-88A precursor at 600°C , the obtained product is standard cubic Fe_3O_4 (joint committee on powder diffraction standards, JCPDS No. 65–3107). However, by the addition of Li_2CO_3 , as-prepared samples exhibit different diffraction peaks from the blank sample. LFO-0.01 and LFO-0.02 show nearly the same XRD patterns assigning to a cubic LiFeO_2 phase (JCPDS No. 17–0938), except all the diffraction peaks are left shifted compared with the standard pattern (Figure 1b). From the enlarged region, LFO-0.01 shows a broader and more left-shifted (200) diffraction peak, indicating the increased lattice parameters than those of LFO-0.02 and LFO-0.03.^[46] In addition, obvious Li_2CO_3 impurity can be seen in the LFO-0.03 pattern, proving that this ratio of lithium and precursor is excessive to form the LiFeO_2 . The Li/Fe ratio of as-prepared LFO-0.01 and LFO-0.02 is determined as 0.43 and 0.87 by inductively coupled plasma optical emission spectrometer (ICP-OES), respectively. As shown in Figure S2a (Supporting Information), the weight of MIL-88A precursor finally remains at 33.51% after the thermogravimetric test, which can be considered as Fe_2O_3 formed by the precursor pyrolysis in air. Based on this result, the Fe content of the precursor would be calculated. Combined with the Li/Fe ratio in the preparation process, the molar ratio of Li/Fe in LFO-0.01 can also be further calculated to be about 0.43, which is consistent with the ICP-OES results. Thus, the chemical formula of LFO-0.01 is $\text{Li}_{0.43}\text{FeO}_{2-x}$. This is a typical nonstoichiometric compound with numerous structural defects, resulting in the left-shifted diffraction peaks and increased electrons/ions conductivity.

The structures and morphologies of the as-prepared samples are observed by scanning electron microscope (SEM) and transmission electron microscope (TEM). As shown in Figure S3 (Supporting Information), MIL-88A precursor displays one-dimensional sharp cone microrod morphology with about 6–10 μm in length and 300–500 nm in diameter. After direct

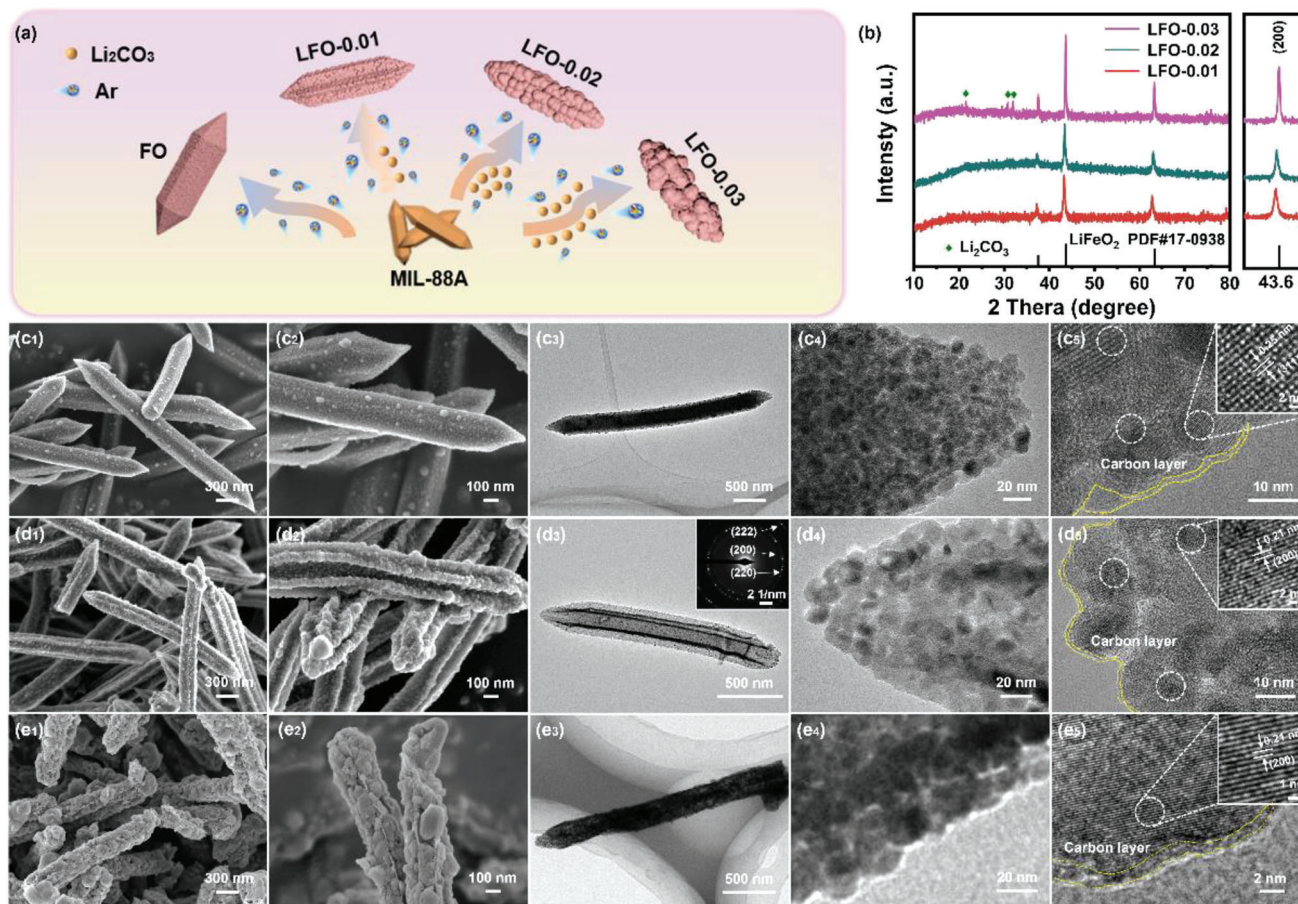


Figure 1. a) Schematic diagram of the preparation processes. b) XRD patterns and SEM, TEM, and HRTEM images of c) FO, d) LFO-0.01, and e) LFO-0.02.

heat treatment, FO inherits the microrod morphology with a rough and porous surface, which is assembled by countless nanoparticles (Figure 1c₁,c₂). TEM image depicted in Figure 1c₃ further shows the solid rod characterization. The primary particles with a diameter of 15 nm are enclosed with an amorphous carbon layer to tolerate the volume expansion and improve the conductivity (Figure 1c₄). Moreover, the clear and parallel lattice fringes with an interplanar distance of 0.25 nm are assigned to the (311) facet of cubic Fe₃O₄. Remarkably, when slight Li₂CO₃ is added and calcined together with the precursor, the rod structure of as-prepared LFO-0.01 shrinks inwardly and forms regular cavities, which can be described as slender carambola-like structure (Figure 1d₁,d₂). In Figure 1d₃, the “keels” supporting a slender carambola-like structure can be clearly observed. LFO-0.01 is also assembled by lots of primary particles and coated with carbon layer, in line with the common morphology decomposition from the MOF precursor (Figure 1d₄). Due to the same precursor utilized, the carbon content of as-prepared samples could be calculated to about 19.64 wt% according to the weight loss of FO. The diameter of LFO-0.01 primary particles is similar to the FO counterpart, indicating that the slight addition of lithium salt does not affect their grain size. Furthermore, SAED pattern exhibits the typical polycrystal feature with a series of rings, agreeing with the (200), (220), and (222) crystal plane of crystal defective LiFeO₂.^[46]

The lattice fringes with a spacing of 0.21 nm belong to the (200) plane of LFO-0.01. With the increase of lithium carbonate, the morphology of as-prepared LFO-0.02 (Figure 1e₁,e₂) and LFO-0.03 (Figure S4, Supporting Information) has been changed gradually. From the TEM images in Figure 1e₃,e₄, the voids in the carambola-like structure have been occupied by the growth primary particles with a diameter of about 25 nm. The increasing grain size of primary particles eventually leads to the collapse of a slender carambola-like structure. HRTEM image of LFO-0.02 (Figure 1e₅) demonstrated that the increased lithium salt addition would not change its interplanar spacing. However, profiles of lattice fringes intensity (Figure S5, Supporting Information) indicate that slight lithium promotes the formation of spot defects, and the number of defects decreases with increasing lithium addition.^[47] N₂ adsorption-desorption isotherms of as-prepared samples are depicted in Figure S6 (Supporting Information). Brunauer–Emmett–Teller (BET) analyses also verified that the voids in the carambola-like structure have been occupied. The specific surface area of LFO-0.02 (95.45 m² g⁻¹) and LFO-0.03 (85.25 m² g⁻¹) is obviously lower than that of LFO-0.01 (116.73 m² g⁻¹) and FO (103.07 m² g⁻¹). The larger specific surface area can provide more active sites to promote the Li⁺/electrons transfer rate, which would result in the improved rate performance.

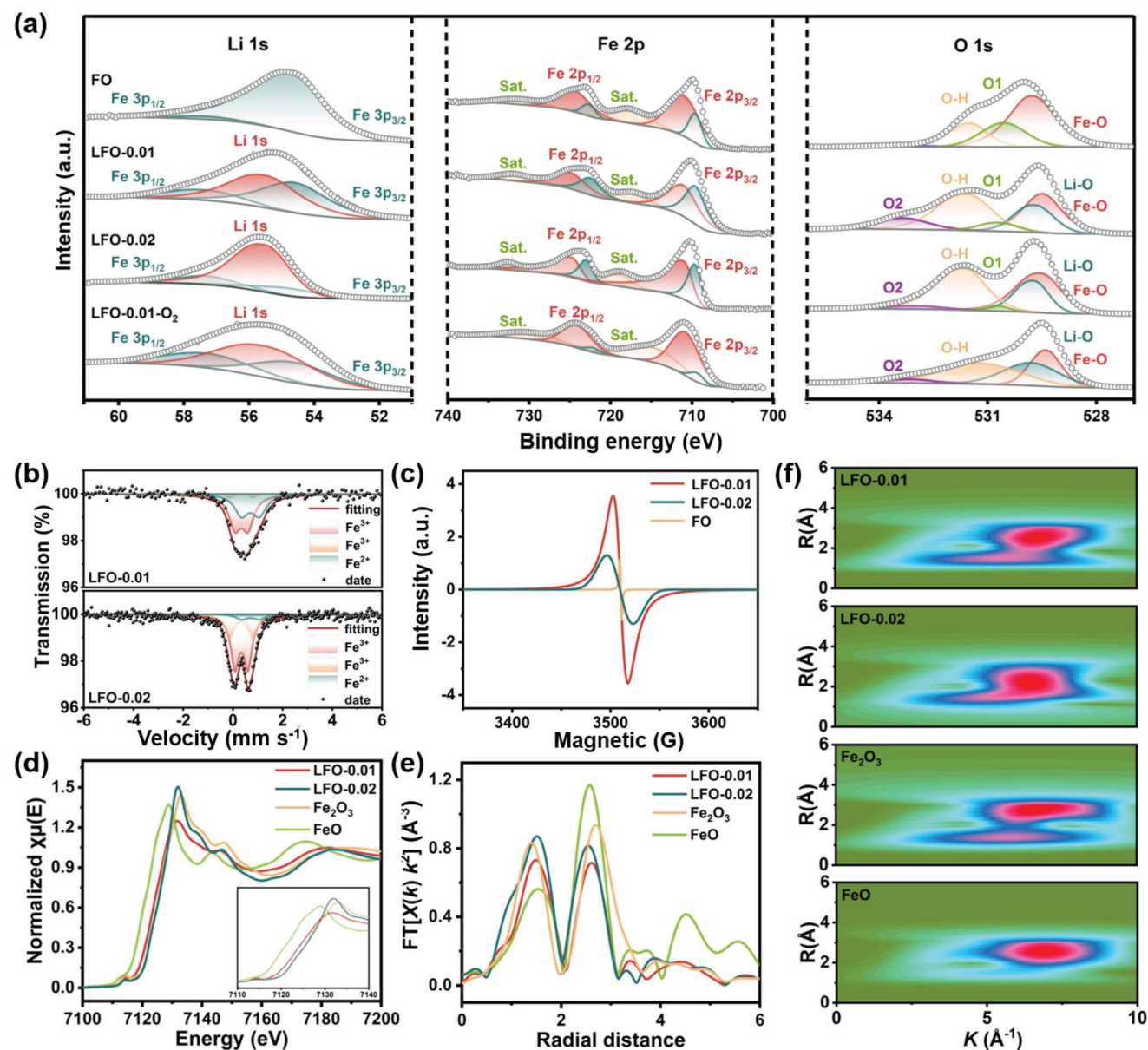


Figure 2. a) XPS spectra of Li 1s, Fe 2p, and O 1s. b) Mössbauer spectroscopy of LFO-0.01 and LFO-0.02; c) EPR results; d) Fe K-edge XANES spectra of LFO-0.01, LFO-0.02, Fe₂O₃, and FeO. e) Fourier transforms of d) Fe K-edge EXAFS spectra and f) the wavelet transform contour plots at the Fe K-edge of FO-0.01, LFO-0.02, Fe₂O₃, and FeO.

X-ray photoelectron spectroscopy (XPS) was used to investigate the surface element composition and chemical state of as-prepared samples. As shown in Figure S7 (Supporting Information), all the XPS survey spectra exhibit the similar profile, which verify the presence of Fe, O, and C in the samples. Because of the binding energy Li 1s is close to that of Fe 3p, the peak of Li 1s would be overlapped in the survey spectra. In **Figure 2a**, the spectrum of FO can be deconvoluted into two peaks, ascribed to Fe 3p_{3/2} and Fe 3p_{1/2}, respectively. In the spectra of LFO-0.01, LFO-0.02, and LFO-0.01-O₂, the profiles can be divided into Fe 3p_{3/2}, Fe 3p_{1/2}, and Li 1s, respectively, demonstrating the presence of Li element. The higher Li 1s peak intensity of

LFO-0.02 means higher content of lithium compared with LFO-0.01. As revealed by the Fe 2p spectra, all the samples exhibit a pair of broad satellite peaks and two pairs of distinct peaks located at 709.5/722.4 and 710.9/724.6 eV, corresponding to the Fe²⁺ 2p_{3/2}/2p_{1/2} and Fe³⁺ 2p_{3/2}/2p_{1/2}, respectively.^[48] Owing to the reduction of carbon coating layer, the abundance of Fe²⁺ on the surface of FO, LFO-0.01, and LFO-0.02 could induce certain structural defects, which is beneficial to improve the ion/electron conductivity.^[49] The O 1s spectrum of FO could be fitted as Fe–O bond (529.5 eV), C–O bond (O1, 530.7 eV, detected from the incomplete reduction of carbon coating layer), hydroxyl group (531.5 eV), and absorbed oxygen, respectively. The Fe–O bond,

Li–O bond (529.7 eV), C–O bond, hydroxyl group, and absorbed oxygen (O₂) can be observed from the LFO-0.01 and LFO-0.002 spectrums. According to Figure S1b (Supporting Information), LFO-0.01-O₂ is a mixture of LiFeO₂ and Fe₂O₃. The spectrum of LFO-0.01-O₂ displays four peaks belonging to the Fe–O bond, Li–O bond, hydroxyl group, and absorbed O₂. The carbon coating layer was oxidized during the heat-treatment in air. Moreover, the high ratio of hydroxyl peak means a strong coupling between cationic vacancies and the hydroxyl species.^[32] In terms of the charge balance principle, the Fe³⁺/Fe²⁺ ratio is an important prerequisite for the verification of x value in LFO-0.01. XPS cannot reflect the intrinsic valence state of materials because of its limited detection depth. Mössbauer spectroscopy has been considered as a powerful tool to estimate the valence state, coordination number of chemical bonds, crystal structure, electron density, and magnetic properties.^[50] As shown in Figure 2b, Mössbauer spectrums of LFO-0.01 and 0.02 exhibit obviously different profiles, owing to the different lithium salt addition. Both LFO-0.01 and LFO-0.02 Mössbauer spectroscopy could be fitted as three doublet peaks with an isomer shift of 0.3379, 0.3426, and 0.7028 mm s⁻¹, which belonged to the valence site of Fe³⁺, Fe³⁺, and Fe²⁺, respectively.^[50] The detailed site parameters of two samples are listed in Table S1 (Supporting Information). After fitting the area of split peaks, the Fe³⁺/Fe²⁺ ratio of LFO-0.01 can be calculated as about 1.44. Further combined with the Li/Fe ratio, the x value can be estimated as 0.49. The chemical formula of LFO-0.01 would be determined to Li_{0.43}FeO_{1.51}. Similarly, the chemical formula of LFO-0.02 is identified as Li_{0.87}FeO_{1.89}.

Electron paramagnetic resonance (EPR) is a physical method to detect the unpaired electron in materials with defects/vacancies by the g value under various chemical environments. The strong symmetrical EPR peaks of FO, LFO-0.01, and LFO-0.02 with a g value of 2.003, 2.001, and 2.001 are observed in Figure 2c, respectively, which meant the existence of electrons captured by structural vacancies. The g value of 2.003 is evidence of oxygen vacancies, meaning that LFO-0.01 and LFO-0.02 possessed the different type of vacancies from the FO counterpart.^[32] It's worth noting that the intensity of ERP peak corresponds to the concentration of unpaired electrons.^[29] LFO-0.01 delivers the highest defect concentration which would benefit the electrons/ions transport. To further analyze the structure of LFO-0.01 and LFO-0.02, the Fe K-edge X-ray absorption near edge structure (XANES) and Fourier-transformed extended X-ray absorption fine structure (FT-EXAFS) were carried out. The K-edge absorption energy of LFO-0.01 and LFO-0.02 lines are between that of FeO and Fe₂O₃ (Figure 2d). From the enlarged absorption edges, the average iron valence of LFO-0.02 is higher than that of LFO-0.01, implying more Fe³⁺ content coupled with the more lithium salt addition. The FT-EXAFS spectrums of LFO-0.01 and LFO-0.02 depicted in Figure 2e present the typical Fe–O bond with one chief peak located at 1.47 Å, one shoulder peak (Fe–Fe bond) at 2.62 Å.^[51] The intensity of peaks in R space reflects the coordination relationship of the corresponding bonds.^[52,53] According to the minimum intensity of shoulder peak, the coordination number of Fe in LFO-0.01 is reduced, which would infer that the defect type in LFO-0.01 is Fe vacancies.^[54] Additionally, the enlarged wavelet transform EXAFS maximum profile indicated that LFO-0.01 delivered more diverse coordination environments than the

counterparts due to the Fe vacancies,^[49,55] which would improve its electrochemical performances. In the process of calcination to form LiFeO₂, the reduced Fe²⁺ by carbon layer would tend to occupy the Li⁺ sites in the case of insufficient lithium addition, which induced cation vacancies compensation to maintain the electrical neutrality.^[56] This tendency decreases with the increase of Li₂CO₃ addition.

Density functional theory (DFT) calculations were conducted to understand the structural features of LFO-0.01 with Fe vacancies. A 2 × 2 × 2 Li₁₆Fe₁₆O₃₂ supercell structure containing 64 atoms was constructed. To generate Fe²⁺, the numbers of lithium and iron atoms are purposefully adjusted in the unit cell to balance the valence and keep the cubic structure. However, their positions are still randomly generated. Based on the practical atom ratio of Li/Fe and the content ratio of Fe³⁺/Fe²⁺, the geometrically optimized models of LFO-0.01 and LFO-0.02 would be approximated to Li₉Fe₂₁O₃₂ and Li₁₅Fe₁₇O₃₂, respectively (Figure 3a,b). There are two Fe vacancies in the Li₉Fe₂₁O₃₂ supercell structure. The calculated total density of states (TDOS) and partial density of states (DOS) of Fe are depicted in Figure 3c. By the creation of Fe vacancies, continuous and obvious states of Fe d orbital near the Fermi level could be observed, which let transportation of electrons much easier than that of Li₁₅Fe₁₇O₃₂.^[25,46] Besides, the DOS of Li and O further demonstrate that Fe is a key role in the variation of models' DOS near the Fermi level (Figure S8, Supporting Information). Moreover, the lithium-ion migration energy barrier in Li₉Fe₂₁O₃₂ is only 1.35 eV, which is much smaller than those of Li₁₅Fe₁₇O₃₂ (1.74 eV), LiFeO₂ (1.80 eV), and Fe₃O₄ (1.96 eV), further demonstrating more easily Li⁺ migration process in Li₉Fe₂₁O₃₂ unit cells. Due to the DFT calculation results, the presence of Fe vacancies in the structure would not only modulate the electronic structure to improve electrical conductivity of LFO-0.01, but also promote the Li⁺ diffusion to accelerate charge storage processes simultaneously.

The electrochemical performances of as-prepared samples were measured by CR2032 half-coin cells. As shown in Figure 4a, LFO-0.01 delivers the first discharge and charge capacity of 1352 and 1173 mAh g⁻¹, respectively, with an ICE of 86.78%. As the counterpart, LFO-0.02 (Figure 4b) synthesized with double the amount of Li₂CO₃ exhibits a lower capacity (1053/853 mAh g⁻¹) and ICE (81.06%), indicating that increasing the amount of Li₂CO₃ would limit its electrochemical activity. However, both LFO-0.01 and LFO-0.02 possess the higher ICE than that of FO (68.24%, Figure 4c) electrode. Overlapped discharge–charge curves demonstrate all of the as-prepared samples have good lithium intercalation/deintercalation reversibility. Moreover, initial cyclic voltammetry (CV) curves of as-prepared electrodes at the scan rate of 0.1 mV s⁻¹ in the voltage range of 0.005–3 V are depicted in Figure S9 (Supporting Information), which accorded with the typical lithiation/delithiation behavior of Fe-based anode materials. During the first discharge, the obvious cathodic peak located at 0.6 V is the reduction of Fe³⁺/Fe²⁺ and the formation of Li₂O. In the anodic scan, a broad peak at around 1.68 V can be assigned to the delithiation and the Fe⁰ oxidation.^[4,11,46] The well-overlapped cathodic and anodic peaks in the next three cycles mean their excellent reversible lithium storage performance.

Figure 4d depicts the cycling performance and coulombic efficiency of as-prepared samples at a current density of 0.5 A g⁻¹. Impressively, the LFO-0.01 electrode remained the discharge

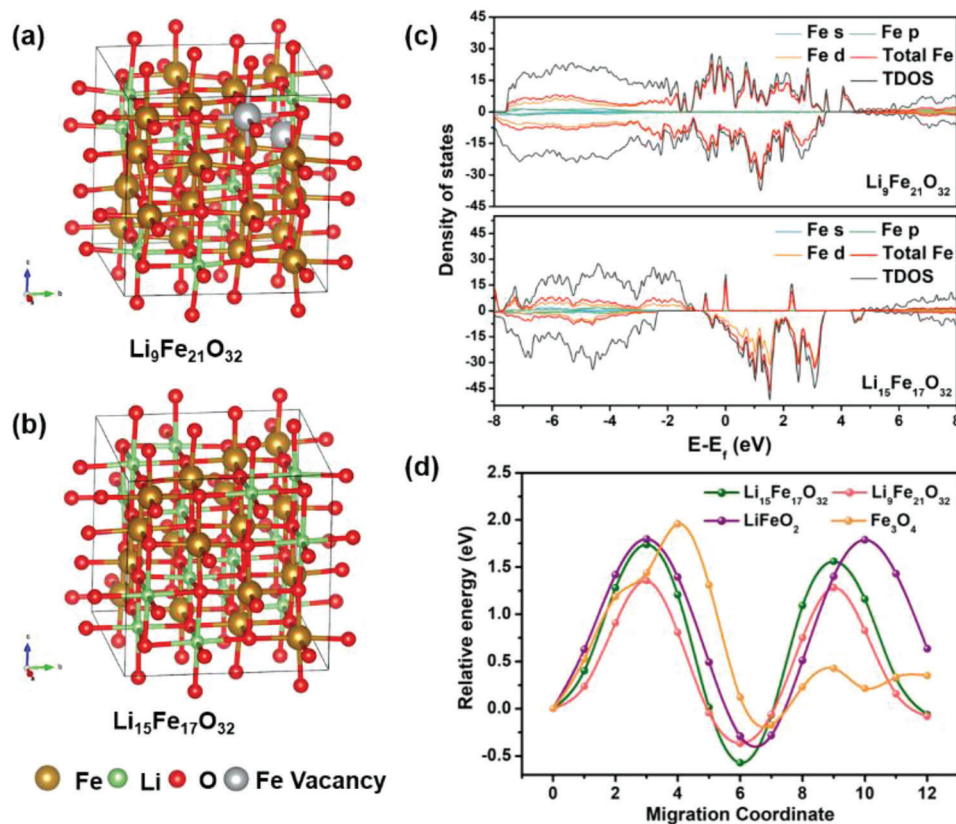


Figure 3. The structural models of a) $\text{Li}_9\text{Fe}_{21}\text{O}_{32}$ and b) $\text{Li}_{15}\text{Fe}_{17}\text{O}_{32}$. c) Density of state of two models of Fe. d) Migration energy profiles of Li^+ in $\text{Li}_9\text{Fe}_{21}\text{O}_{32}$, $\text{Li}_{15}\text{Fe}_{17}\text{O}_{32}$, LiFeO_2 , and Fe_3O_4 .

specific capacity of 884 mAh g^{-1} after 500 cycles, which is much higher than that of LFO-0.02 (445 mAh g^{-1}), LFO-0.03 (203 mAh g^{-1} , Figure S10a, Supporting Information) and FO (118 mAh g^{-1}) electrodes. The dQ/dV curves of LFO-0.01 at different cycles in Figure S11 (Supporting Information) show the similar profiles, meaning its high reversibility of lithium storage. Moreover, the electrochemical performances of LFO-0.01 are obviously superior to the reported Fe-based anode materials in cycling capacity and ICE (Figure 4e).^[57–61] As shown in Figure 4f and Figure S10b (Supporting Information), LFO-0.01, LFO-0.02, and LFO-0.03 exhibit the improved rate performances at high current density, which is attributed to their increased Li^+ /electrons diffusion rates. The LFO-0.01 electrode shows the best rate performance, and delivers the specific capacity of 1000, 930, 860, 753, 658, 545, 357, 145, and 1148 mAh g^{-1} at 0.05, 0.1, 0.2, 0.5, 1, 2, 5, 10, and back to 0.05 A g^{-1} respectively. However, the diffusion contribution ratio of LFO-0.01 is larger than that of FO, meaning the improved diffusion kinetics of LFO-0.01 (Figure S12, Supporting Information). This interesting phenomenon is reversed to the reported modified iron oxide anodes.^[62,63] The increased diffusion contribution ratio of LFO-0.01 would be attributed to the modulated charge distribution by the presence of Fe vacancies, and consequently weakened the electrostatic interaction to promote Li^+ diffusion in the LFO-0.01 structure.^[64] Galvanostatic intermittent titration technique (GITT) method is carried out to estimate the lithium-ion diffusion coefficient of as-prepared samples. As shown in Figure 4g, all the GITT curves profiles

are corresponding to their discharge–charge curves. The lithium diffusion coefficient (D_{Li}) of three electrodes can be calculated according to the following Equation (1) (the meaning of parameters is supplemented in Figure S13, Supporting Information).^[25] During the discharge–charge periods (Figure 4k), all of the electrodes display the same variation trends. And the LFO-0.01 owns the highest D_{Li} to promote the rate performance.

$$D_{\text{GITT}} = \frac{4}{\pi\tau} \left(\frac{m_{\text{B}} V_{\text{M}}}{M_{\text{B}} S} \right)^2 \left(\frac{\Delta E_{\text{s}}}{\Delta E_{\text{t}}} \right)^2 \quad (1)$$

Furthermore, electrochemical impedance spectroscopy (EIS) is used to evaluate the resistance of charge transfer (R_{ct}) at different cycles. All the Nyquist plots (Figure S14, Supporting Information) deliver two semicircles and a line in the middle and high-frequency regions at 100th cycle, representing the surface film resistance (R_{f}), R_{ct} , and Warburg impedance (Z_{w}), respectively.^[65] Compared with the counterparts (the R_{ct} of FO and LFO-0.02 is 2046 and 192.5Ω , respectively), the smallest R_{ct} of LFO-0.01 at 100th cycle (156.6Ω) would be attributed to the presence of Fe vacancies, which promoted the charge transfer processes. With the increase of cycles, the impedances of the three electrodes exhibit similar decreasing trends, implying the continuous improvement in charge storage kinetics. GITT and EIS analyses clearly demonstrate that the existence of Fe vacancies in LFO-0.01 facilitates ion diffusion and charge transfer during the charge–discharge processes, which is consistent with the DFT calcula-

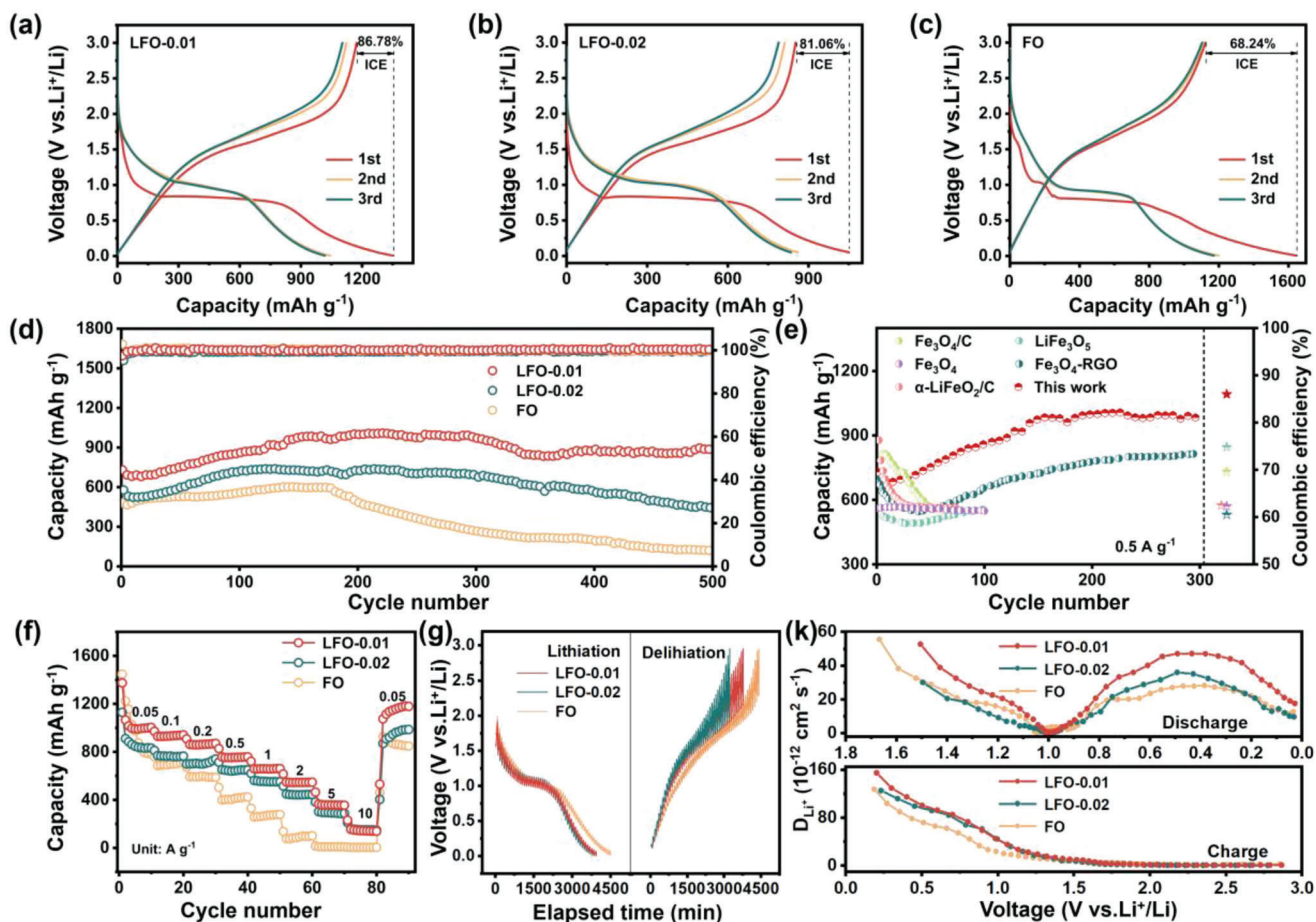


Figure 4. Initial three discharge–charge curves of a) LFO-0.01, b) LFO-0.02, and c) FO. d) Long-term cyclic performances under the current density of 0.5 A g^{-1} , f) rate performances, g) GITT curves and k) Li^+ diffusion coefficient at different states of LFO-0.01, LFO-0.02, and FO. e) Comparison of cyclic performance and initial coulombic efficiency (ICE) between LFO-0.01 and reported Fe-based anodes.

tion results. Besides, the LFO-0.01 and FO batteries after 50 cycles at 0.5 A g^{-1} have been dissected and characterized by SEM to check the morphology evolution. Evidently, LFO-0.01 still retains the slender carambola-like morphology with the thin SEI film on the surface (Figure S15a,b, Supporting Information). As the counterpart, FO microrods display the enlarged diameter, rough surface, and pulverized particles (Figure S15d,e, Supporting Information), which proved that the structural stability of LFO-0.01 is better than that of FO. The SEM images of the electrode cross profile depicted in Figure S15c (Supporting Information) show that the thickness increase of LFO-0.01 electrode is only about 40%, far less than that of FO (increased by 120%, Figure S15f, Supporting Information). According to the above results, the impressive improvement of LFO-0.01 would be attributed to the slender carambola-like structure and the Fe vacancies induced by the non-stoichiometric design. These structural features not only alleviate the volume expansion and accelerate ion/electron diffusion rates during the monotonous cycles, but also reduce the irreversible capacity loss and endow more active sites to obtain the high reversible capacity.

Ex situ XPS and TEM are performed at different discharged–charged states in the Li^+ half-cells to explain the lithium storage

mechanism. After first discharged to 2 V, the Li 1s spectrum (Figure 5b₁) could be divided into the ROCO_2Li , Li_2CO_3 , Li_2O , and LiF peaks, representing the formation of SEI film and the reduction of iron ions. Limited by the detection depth of XPS, the weak signals of Fe element have been collected, which were affected by the formed SEI film (Figure 5c). Thus, the interference of Fe 3p signal in Li 1s can be ignored by the low intensity of Fe 2p signal. The relative content of Li_2O reaches the maximum at 0.005 V, and gradually decreases at the charge stage. At the end of the first charge (Figure 5b₂), the residual signal of Li_2O is mainly attributed to the SEI film and irreversible Li_2O . Fe^0 signal intensity is getting higher with the increasing discharge depth. At 0.005 V (Figure 5c₃), an obvious Fe^{2+} peak still exists, implying the incomplete reduction processes. During the charging process, the content of Fe decreases continuously, and a slight Fe^0 has found at a cut-off voltage of 3 V (Figure 5c₅), indicating that the charging process was also incomplete, and foreshadowed for the subsequent capacity rising. At the following cycles, these active materials would be gradually exposed to enhance the lithium storage ability. In O 1s spectrums (Figure 5d), the change tendency of Fe–O and Li–O bonds are consistent with analyses of ex situ Li 1s and Fe 2p spectrums. As shown in Figure 5e,

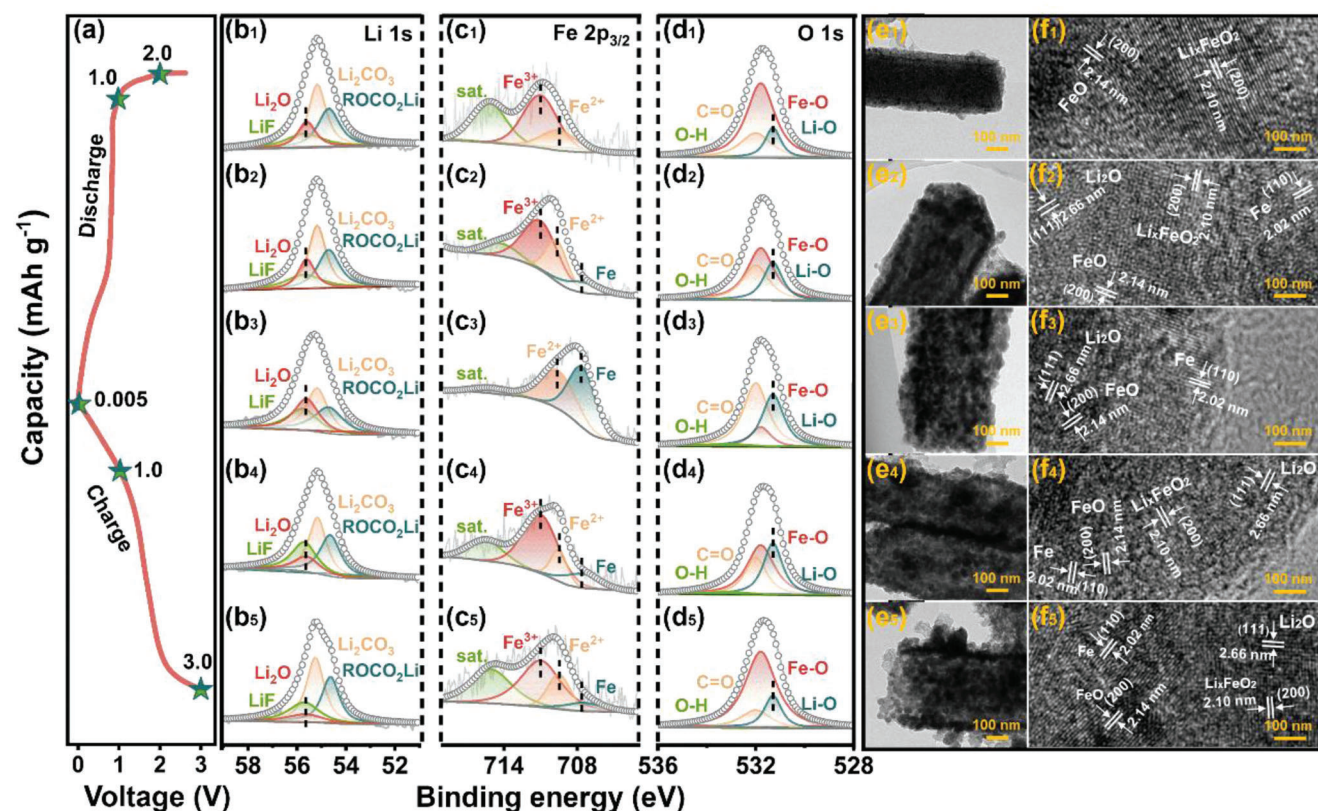


Figure 5. a) Initial charge–discharge curve, b) Li 1s spectrums, c) Fe 2p_{3/2} spectrums, d) O 1s spectrums. e) TEM images and f) HRTEM images of LFO-0.01 at different states.

the one-dimensional morphology of LFO-0.01 can be clearly observed at different states. Furthermore, at the first discharged to 2 V, (200) plane of FeO and (200) plane of Li_xFeO₂ is observed in the HRTEM image (Figure 5f₁). The (110) plane of Fe can be found in the following discharged at 1 V (Figure 5f₂). Li_xFeO₂ is absent at discharged of 0.005 V, and reappears at the charged of 1 and 3 V, implying the conversion reaction between Li_xFeO₂ and FeO.

Moreover, the anode material had not been reduced completely in the first discharge process, according to the ex situ XPS and TEM analyses. The unreduced LFO-0.01 may play a critical role in the charging process. To verify this conjecture, DFT calculations using the above models are carried out. **Figure 6a,b** displays the optimized structure of Li₂O adsorbed on the (010) plane of Li₉Fe₂₁O₃₂ and Li₁₅Fe₁₇O₃₂, respectively. The adsorption energy (E_{ads}) calculation results show that the E_{ads} on Li₉Fe₂₁O₃₂ surface (the model of LFO-0.01) is significantly lower than that of Li₁₅Fe₁₇O₃₂ (the model of LFO-0.02), inferring that the presence of Fe vacancies acts as the active site to promote the capture of Li₂O. This result may be the critical factor for the higher ICE of LFO-0.01 than LFO-0.02. Figure 6c depicts the Gibbs free energy diagram of Li₂O cluster decomposition and formation of Li_xFeO_y on the surface of Li₉Fe₂₁O₃₂ during the first charge process. From the calculated energy diagram, the reaction between Li₂O and Fe on the surface of Li₉Fe₂₁O₃₂ (presence of the Fe vacancies) to form Li_xFeO_y goes through five steps. After the first step of Li₂O adsorption, ΔG of transient state (TS) 1 and TS2 are

only 0.05 and 0.04 eV, respectively. Besides, the ΔG of the whole reaction is -1.20 eV, indicating the thermodynamically spontaneous reaction. DFT calculations indicate that Fe vacancies, as active sites, would capture Li₂O, catalyze the reaction between Fe and Li₂O, and reduce the amount of irreversible Li₂O simultaneously, which is regarded as the main factor to the ICE improvement. Hence, the ICE improvement processes can be illustrated in Figure 6d. In the first lithiation process, LFO-0.01 reduced the lithium consumption compared with FO, which is reflected in the lower first irreversible discharge capacity. At the subsequent charge process, decreasing the amount of irreversible Li₂O and catalyzing more Li₂O to participate in the following reaction with Fe can directly increase the charge capacity, and improve the ICE of LFO-0.01 consequently.

Furthermore, the LiFePO₄||LFO-0.01 coin full-cells are assembled by using the commercial LiFePO₄ as cathode with the negative/positive capacity (N/P) ratio of 1.2 (**Figure 7a**), encouraged by the outstanding electrochemical performances of LFO-0.01 electrode in a half-cell. The electrochemical performances of commercial LiFePO₄ in half-cells are exhibited in Figure S16 (Supporting Information). As shown in Figure 7b, the voltage window of the LiFePO₄||LFO-0.01 full-cell is set between 0.5 and 3.5 V. The capacity of the full-cell is calculated based on the weight of the cathode material. In the evaluation of rate performance (Figure. 7c), LiFePO₄||LFO-0.01 full-cell delivers a specific capacity of 134, 120, 105, 80, 133, and 113 mAh g⁻¹ at the current density of 0.1, 0.2, 0.3, 0.5, back to 0.1, and 0.2 mA cm⁻², respectively,

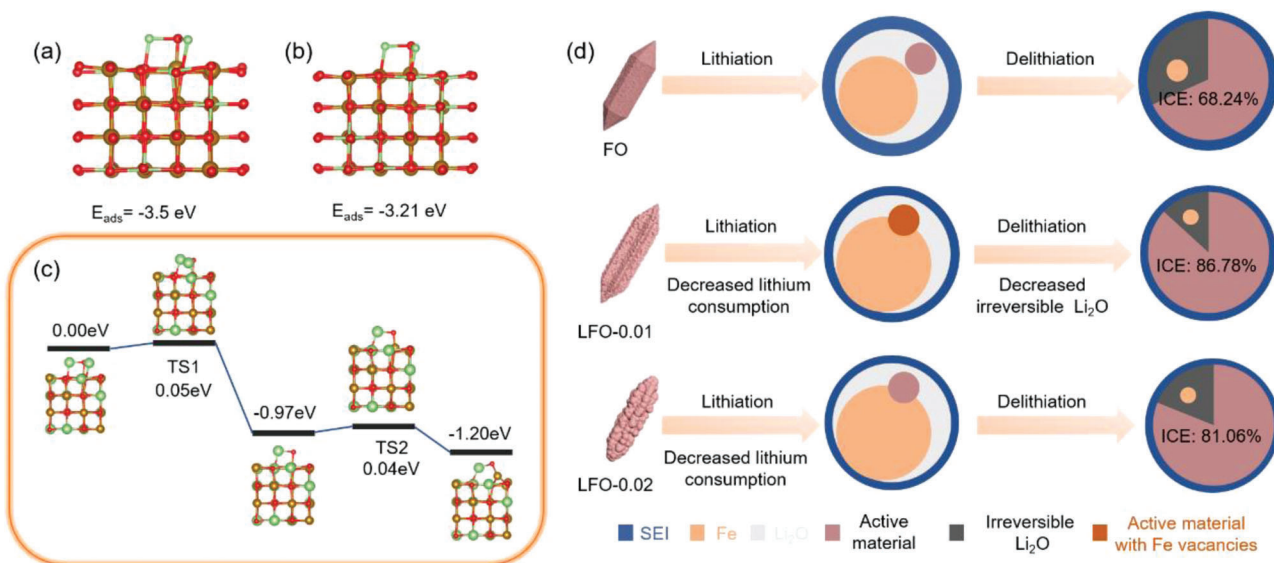


Figure 6. Optimized structure of Li_2O adsorbed on the (010) plane of a) $\text{Li}_9\text{Fe}_{21}\text{O}_{32}$ and b) $\text{Li}_{15}\text{Fe}_{17}\text{O}_{32}$. c) The Gibbs free energy diagram of Li_2O cluster decomposition on the surface of $\text{Li}_9\text{Fe}_{21}\text{O}_{32}$ during the first charge process. d) Schematic diagram of initial coulombic efficiency (ICE) improvement processes.

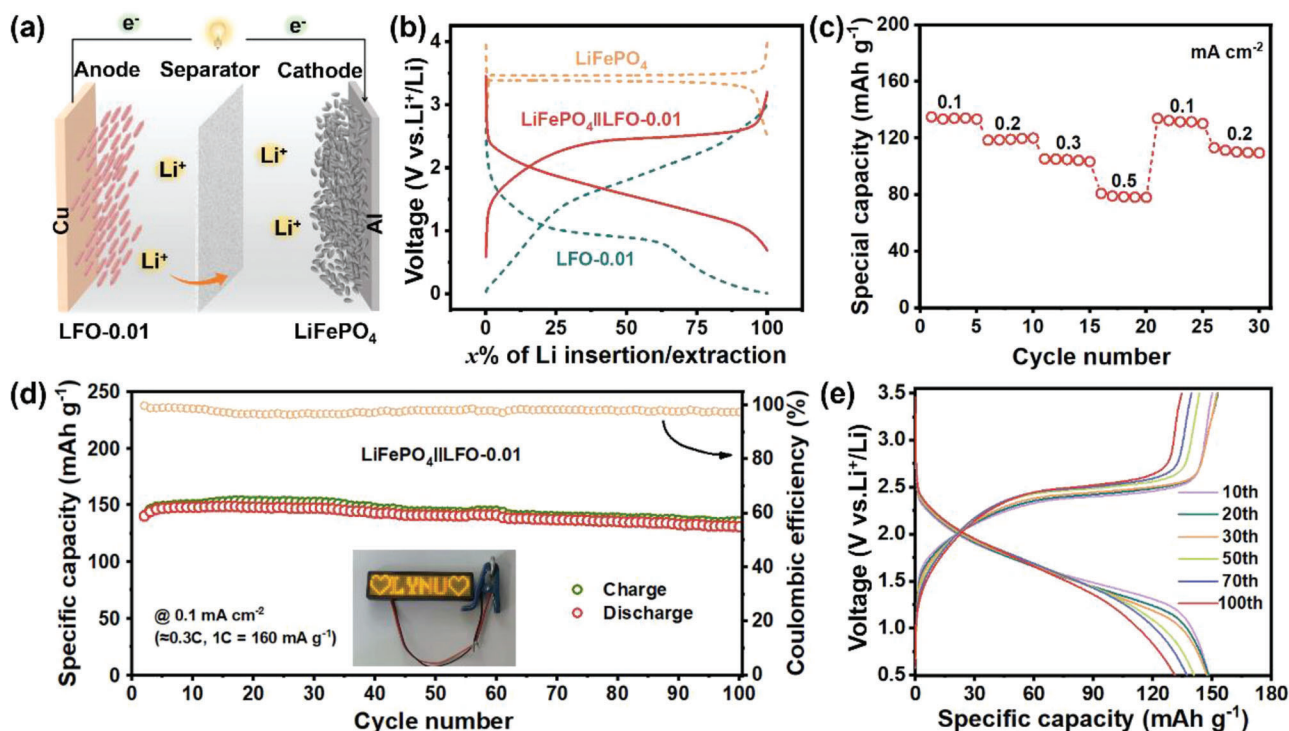


Figure 7. a) Schematic illustration of the full-cell configuration. b) Typical charge–discharge curves of $\text{LiFePO}_4||\text{LFO-0.01}$ full-cell. The c) rate performance, d) cyclic performance, and e) charge–discharge curves at different cycles of $\text{LiFePO}_4||\text{LFO-0.01}$ full-cell.

which indicates the good rate capability of $\text{LiFePO}_4||\text{LFO-0.01}$ full-cell. At the following cyclic test (Figure 7d), $\text{LiFePO}_4||\text{LFO-0.01}$ full-cell shows superior cyclic stability with a high capacity of 131 mA h g^{-1} , 99.2% capacity retention and close to 100% coulombic efficiency after 100 cycles at 0.1 mA cm^{-2} ($\approx 0.3 \text{ C}$, 1

$\text{C} = 160 \text{ mA g}^{-1}$). The inset in Figure 7d is a digital photo of “LYNU” LEDs device lighted by a coin full-cell. Besides, the monotonous charge–discharge plateaus at different cycles (Figure 7e) demonstrate that $\text{LiFePO}_4||\text{LFO-0.01}$ full-cell would deliver a stable voltage for electrical equipment.

3. Conclusion

In summary, a type of lithium iron oxide with hollow slender carambola-like structure and Fe vacancies has been synthesized by the thermal reaction between MIL-88A precursor and Li_2CO_3 . The structure features and electrochemical performances of as-synthesized lithium iron oxides have been obviously affected by the addition of lithium salt. A small amount of Li_2CO_3 leads to the formation of hollow LFO-0.01 with Fe vacancies during the heat-treatment process. DFT calculations show that the presence of Fe vacancies accelerates the transport rate of lithium ions and catalyzes more decomposition of Li_2O to participate in the reaction with Fe. Thus, LFO-0.01 delivers the superior performances in lithium storage, including the high ICE (86.78%) and stable cyclic property (884 mAh g^{-1} after 500 cycles at 0.5 A g^{-1}). The $\text{LiFePO}_4\|\text{LFO-0.01}$ coin full-cells also exhibit the high capacity (131 mAh g^{-1}) and stable cyclic performance (99.3% retention after 100 cycles). This work would encourage other transition metal oxides with conversion-type lithium storage mechanism to improve their electrochemical performances.

Supporting Information

Supporting Information is available from the Wiley Online Library or from the author.

Acknowledgements

N.W., J.S., and K.Y. contributed equally to this work. The authors acknowledge the financial support from the Natural Science Foundations of China [Nos. 51904152 and 21965033], Natural Science Foundations of Henan Province [No. 222300420502], the Program for Science and Technology Innovation Talents in Universities of Henan Province [No. 20HASTIT020], and the Key Science and Technology Program of Henan Province [No. 222102240044].

Conflict of Interest

The authors declare no conflict of interest.

Data Availability Statement

Research data are not shared.

Keywords

electronic structure modulation, high initial coulombic efficiency, iron vacancies, lithium iron oxide, lithium-ion batteries

Received: November 9, 2022
Revised: December 15, 2022
Published online:

[1] B. Wang, Y. Wei, H. Fang, X. Qiu, Q. Zhang, H. Wu, Q. Wang, Y. Zhang, X. Ji, *Adv. Sci.* **2021**, *8*, 2002866.

- [2] R. C. K. Reddy, X. Lin, A. Zeb, C. Su, *Electrochem. Energy Rev.* **2022**, *5*, 312.
- [3] Z. Na, G. Huang, F. Liang, D. Yin, L. Wang, *Chem. - Eur. J.* **2016**, *22*, 12081.
- [4] D. Xie, H. Li, Y. Shi, W. Diao, R. Jiang, H. Sun, X. Wu, W. Li, C. Fan, J. Zhang, *Chem. - Eur. J.* **2020**, *26*, 853.
- [5] T. Jiang, F. Bu, X. Feng, I. Shakir, G. Hao, Y. Xu, *ACS Nano* **2017**, *11*, 5140.
- [6] F. Zheng, M. He, Y. Yang, Q. Chen, *Nanoscale* **2015**, *7*, 3410.
- [7] N. Mahmood, T. Tang, Y. Hou, *Adv. Energy Mater.* **2016**, *6*, 1600374.
- [8] H. Sun, J. Zhu, D. Baumann, L. Peng, Y. Xu, I. Shakir, Y. Huang, X. Duan, *Nat. Rev. Mater.* **2019**, *4*, 45.
- [9] R. C. K. Reddy, J. Lin, Y. Chen, C. Zeng, X. Lin, Y. Cai, C. Su, *Coord. Chem. Rev.* **2020**, *420*, 213434.
- [10] K. Cao, L. Jiao, H. Liu, Y. Liu, Y. Wang, Z. Guo, H. Yuan, *Adv. Energy Mater.* **2015**, *5*, 1401421.
- [11] N. Wu, W. Tian, J. Shen, X. Qiao, T. Sun, H. Wu, J. Zhao, X. Liu, Y. Zhang, *Inorg. Chem. Front.* **2019**, *6*, 192.
- [12] H. Jiang, L. Huang, Y. Wei, B. Wang, H. Wu, Y. Zhang, H. Liu, S. Dou, *Nano-Micro Lett.* **2019**, *11*, 56.
- [13] H. Liu, S. Luo, D. Hu, X. Liu, Q. Wang, Z. Wang, Y. Wang, L. Chang, Y. Liu, T. Yi, Y. Zhang, A. Hao, *Appl. Surf. Sci.* **2019**, *495*, 143590.
- [14] F. Wang, T. Li, Y. Fang, Z. Wang, J. Zhu, *J. Alloys Compd.* **2021**, *857*, 157531.
- [15] Q. Wang, C. Guo, J. He, S. Yang, Z. Liu, Q. Wang, *J. Alloys Compd.* **2019**, *795*, 284.
- [16] S. Hu, M. Yi, H. Wu, T. Wang, X. Ma, X. Liu, J. Zhang, *Adv. Funct. Mater.* **2022**, *32*, 2111084.
- [17] Q. Li, Y. Zhao, H. Liu, P. Xu, L. Yang, K. Pei, Q. Zeng, Y. Feng, P. Wang, R. Che, *ACS Nano* **2019**, *13*, 11921.
- [18] Y. Wu, Z. Wei, R. Xu, Y. Gong, L. Gu, J. Ma, Y. Yu, *Nano Res.* **2019**, *12*, 2211.
- [19] X. Guo, L. Xiao, P. Yan, M. Li, M. Zhu, J. Liu, *Chin. Chem. Lett.* **2021**, *32*, 3491.
- [20] G. Zhang, T. Xiong, M. Yan, L. He, X. Liao, C. He, C. Yin, H. Zhang, L. Mai, *Nano Energy* **2018**, *49*, 555.
- [21] J. Li, C. Shu, A. Hu, Z. Ran, M. Li, R. Zheng, J. Long, *Chem. Eng. J.* **2020**, *387*, 122678.
- [22] T. Li, K. Liu, G. Nam, M. Kim, Y. Ding, B. Zhao, Z. Luo, Z. Wang, W. Zhang, C. Zhao, J. Wang, Y. Song, M. Liu, *Small* **2022**, *18*, e2200972.
- [23] D. Zu, H. Wang, S. Lin, G. Ou, H. Wei, S. Sun, H. Wu, *Nano Res.* **2019**, *12*, 2150.
- [24] N. Wu, H. Wu, X. Qiao, J. Shen, X. Liu, G. Liu, T. Sun, H. Hou, Y. Zhang, X. Ji, *Electrochim. Acta* **2019**, *299*, 540.
- [25] G. Liu, H. Wu, Q. Meng, T. Zhang, D. Sun, X. Jin, D. Guo, N. Wu, X. Liu, J. Kim, *Nanoscale Horiz.* **2020**, *5*, 150.
- [26] G. Liu, L. Xu, Y. Li, D. Guo, N. Wu, C. Yuan, A. Qin, A. Cao, X. Liu, *Chem. Eng. J.* **2022**, *430*, 132689.
- [27] N. Wu, J. Shen, L. Sun, M. Yuan, Y. Shao, J. Ma, G. Liu, D. Guo, X. Liu, Y. He, *Electrochim. Acta* **2019**, *310*, 70.
- [28] N. Wu, W. Du, X. Gao, L. Zhao, G. Liu, X. Liu, H. Wu, Y. He, *Nanoscale* **2018**, *10*, 11460.
- [29] G. Liu, F. Xiao, T. Zhang, Y. Gu, J. Li, D. Guo, M. Xu, N. Wu, A. Cao, X. Liu, *Appl. Surf. Sci.* **2022**, *597*, 153688.
- [30] N. Wu, W. Du, G. Liu, Z. Zhou, H. Fu, Q. Tang, X. Liu, Y. He, *ACS Appl. Mater. Interfaces* **2017**, *9*, 43681.
- [31] H. Huang, C. Yu, H. Huang, C. Zhao, B. Qiu, X. Yao, S. Li, X. Han, W. Guo, L. Dai, J. Qiu, *Nano Energy* **2019**, *58*, 778.
- [32] X. Chen, M. Yu, Z. Yan, W. Guo, G. Fan, Y. Ni, J. Liu, W. Zhang, W. Xie, F. Cheng, J. Chen, *CCS Chem.* **2021**, *3*, 675.
- [33] B. Liu, Y. Wang, H. Peng, R. Yang, Z. Jiang, X. Zhou, C. Lee, H. Zhao, W. Zhang, *Adv. Mater.* **2018**, *30*, 1803144.
- [34] J. Zhao, Z. Lu, N. Liu, H. Lee, M. T. McDowell, Y. Cui, *Nat. Commun.* **2014**, *5*, 5088.

- [35] M. M. Rahman, J. Wang, M. F. Hassan, Z. Chen, H. Liu, *J. Alloys Compd.* **2011**, 509, 5408.
- [36] P. C. Wang, H. P. Ding, T. Bark, C. H. Chen, *Electrochim. Acta* **2007**, 52, 6650.
- [37] R. Ma, Y. Liu, Y. He, M. Gao, H. Pan, *J. Phys. Chem. Lett.* **2012**, 3, 3555.
- [38] X. Min, G. Xu, B. Xie, P. Guan, M. Sun, G. Cui, *Energy Storage Mater.* **2022**, 47, 297.
- [39] F. Li, Y. Cao, W. Wu, G. Wang, D. Qu, *Small Methods* **2022**, 6, 2200411.
- [40] J. Choi, H. Jeong, J. Jang, A. Jeon, I. Kang, M. Kwon, J. Hong, M. Lee, *J. Am. Chem. Soc.* **2021**, 143, 9169.
- [41] J. Zhao, Z. Lu, N. Liu, H. W. Lee, M. T. McDowell, Y. Cui, *Nat. Commun.* **2014**, 5, 5088.
- [42] J. Zhao, J. Sun, A. Pei, G. Zhou, K. Yan, Y. Liu, D. Lin, Y. Cui, *Energy Storage Mater.* **2018**, 10, 275.
- [43] L. Ren, R. Zheng, B. Zhou, H. Xu, R. Li, C. Zhao, X. Wen, T. Zeng, C. Shu, *Small* **2021**, 17, 2104349.
- [44] X. Liu, L. Zhao, H. Xu, Q. Huang, Y. Wang, C. Hou, Y. Hou, J. Wang, F. Dang, J. Zhang, *Adv. Energy Mater.* **2020**, 10, 2001415.
- [45] H. Xu, R. Zheng, D. Du, L. Ren, R. Li, X. Wen, C. Zhao, T. Zeng, B. Zhou, C. Shu, *Sci. China Mater.* **2022**, 65, 1761.
- [46] Y. Yang, X. Qu, X. Zhang, Y. Liu, J. Hu, J. Chen, M. Gao, H. Pan, *Adv. Mater.* **2020**, 32, 1908285.
- [47] Z. Nie, Z. Tang, D. Jiao, M. Yuan, J. Zhao, Q. Lai, Y. Liang, *ChemCatChem* **2022**, 14, 202101885.
- [48] L. Wang, F. Liu, A. Pal, Y. Ning, Z. Wang, B. Zhao, R. Bradley, W. Wu, *Carbon* **2021**, 179, 327.
- [49] P. Gao, Z. Chen, Y. Gong, R. Zhang, H. Liu, P. Tang, X. Chen, S. Passerini, J. Liu, *Adv. Energy Mater.* **2020**, 10, 1903780.
- [50] H. Aziam, S. Indris, H. B. Youcef, R. Witte, A. Sarapulova, H. Ehrenberg, I. Saadoune, *J. Alloys Compd.* **2022**, 906, 164373.
- [51] Y. Fang, Y. Xue, L. Hui, H. Yu, C. Zhang, B. Huang, Y. Li, *Adv. Sci.* **2022**, 9, 2102721.
- [52] R. Liu, Y. Wang, D. Liu, Y. Zou, S. Wang, *Adv. Mater.* **2017**, 29, 1701546.
- [53] Y. Wang, Y. Zhang, Z. Liu, C. Xie, S. Feng, D. Liu, M. Shao, S. Wang, *Angew. Chem., Int. Ed.* **2017**, 56, 5867.
- [54] Y. Li, J. Huang, X. Hu, L. Bi, P. Cai, J. Jia, G. Chai, S. Wei, L. Dai, Z. Wen, *Adv. Funct. Mater.* **2018**, 28, 1803330.
- [55] Y. Ding, Q. Cheng, J. Wu, T. Yan, Z. Shi, M. Wang, D. Yang, P. Wang, L. Zhang, J. Sun, *Adv. Mater.* **2022**, 34, 2202256.
- [56] B. Koo, H. Xiong, M. D. Slater, V. B. Prakapenka, M. Balasubramanian, P. Podsiadlo, C. S. Johnson, T. Rajh, E. V. Shevchenko, *Nano Lett.* **2012**, 12, 2429.
- [57] Q. Wu, R. Zhao, X. Zhang, W. Li, R. Xu, G. Diao, M. Chen, *J. Power Sources* **2017**, 359, 7.
- [58] X. Hu, S. Xiang, H. Sun, X. Lou, Q. Xiong, X. Lu, H. Qin, Z. Ji, B. Hu, *Nanoscale* **2019**, 11, 11892.
- [59] P. Salimi, O. Norouzi, S. E. M. Pourhosseini, *J. Alloys Compd.* **2019**, 786, 930.
- [60] Y. Shi, K. Wang, H. Li, H. Wang, X. Li, X. Wu, J. Zhang, H. Xie, Z. Su, J. Wang, H. Sun, *Appl. Surf. Sci.* **2020**, 511, 145465.
- [61] M. Büyükyazi, S. Mathur, *Nano Energy* **2015**, 13, 28.
- [62] Z. Zhao, A. R. Akbar, Z. Liu, Y. Lu, Y. Chen, C. Xiong, *Colloids Surf., A* **2022**, 635, 128084.
- [63] Q. Wu, R. Jiang, H. Liu, *Ceram. Int.* **2020**, 46, 12732.
- [64] W. Li, C. Han, Q. Gu, S. L. Chou, J. Z. Wang, H. K. Liu, S. X. Dou, *Adv. Energy Mater.* **2020**, 10, 2001852.
- [65] N. Wu, H. Wu, J. Kim, X. Liu, Y. Zhang, *ChemElectroChem* **2018**, 5, 78.